Inorganic fullerene-type WS$_2$ nanoparticles: processing, characterization and its photocatalytic performance on malachite green

Saurabh Jyoti Hazarika[1] · Dambarudhar Mohanta[1] (ID)

Abstract In this work, we have employed a hydrothermal route for the synthesis of fullerene-type tungsten disulfide (WS$_2$) nanoparticles. X-ray diffraction analysis signifies a hexagonal crystal structure of WS$_2$ with the crystallites experiencing preferred orientations along (002) and (103) planes. The agglomerated nanoparticles and inorganic fullerene (IF)-type structures are apparently observable from the high-resolution electron micrographs. Raman spectrum shows prominent E_{2g}^1 and A_{1g} modes emanating from the IF nano-WS$_2$ system. The Tauc's plot obtained from the optical absorption data predicts a direct band gap of ∼1.91 eV for the nano-WS$_2$ system; whereas, photoluminescence analysis reveals a broad emission peak located at ∼638 nm and is ascribed to the associated transition from the indirect to direct nature of the band gap. The photocatalytic decomposition of malachite green (MG) solution (30 mg/l) by WS$_2$ (100 mg/l) under UV and visible light irradiation has been evaluated. The latter condition exhibited a better photocatalytic response with the MG degradation as high as 71.2%, revealed for 120 min. Photocatalytic and optoelectronic features of IF-type nano-WS$_2$ would bring new insights not only to resolve issues related to environmental hazards, but also in functional devices of technological relevance.

1 Introduction

The pioneering works on atomically thin graphene layers have paved the way for the investigation of 2D layered materials in recent years [1]. The recent research works in the field of graphene has shown some extraordinarily interesting properties including its applicability in the field of bioelectronics for artificial dynamic synapse [2]. Undoubtedly, graphene offers a unique platform in the sense that, with the use of electrical gating Fermi level can be easily tuned along with the band gap opening. The gate-controlled graphene electrode-based random access memory with an adaptable single-electron transistor window has been worked out [3]. Due to the lack of inherent band gap, the electronic components made from graphene cannot be switched on and off in an efficient manner, which gives a low turn on and off time ratios [4]. To overcome this technical limitation, there is an urgent need to exploit other 2D layered materials, known as transition metal dichalcogenide (TMDC) systems. TMDCs have generalized formula MX$_2$, where M is a transition metal element (group IV or V), and X is a chalcogen [5]. In several applications, these materials are advantageous over graphene as they possess sizable band gap, better exfoliation and handling capability, low phonon energy, etc. These materials, in conjunction with other 2D materials, are capable of making high-performance optoelectronic components over a broad spectral range [3, 6]. On the other hand, monochalcogenides of group IV elements (like Ge and Si), which possess black phosphorus-type structure along with other low symmetry TMDC, such as rhenium disulphide (ReS$_2$) and rhenium diselenide (ReSe$_2$) exhibit unique physical properties for numerous applications in the field of nano-electronics, nanophotonics, piezoelectric devices and thermo-electronics [7].

✉ Dambarudhar Mohanta
best@tezu.ernet.in

1 Nanoscience and Soft Matter Laboratory, Department of Physics, Tezpur University, Napaam, Tezpur, Assam 784 028, India

In the past decade, molybdenum disulfide (MoS_2), which is an important member of the family of TMDCs, has received widespread interest among the researchers. MoS_2 has been extensively studied compared to tungsten disulphide (WS_2) counterpart [8–10]. However, WS_2 has not been evaluated in great detail due to insufficient information as regards its physical properties and processibility conditions. WS_2 has drawn research interest owing to exhibition of its matchless value in the field of hydrogen storage, microelectrode material, solid lubrication, catalysis, etc. [11–13]. The crystal structure of WS_2 consists of an S–W–S single-layer bonded Van der Waals force. WS_2 can adopt a single graphite-like structure, or quantum dot nanoparticles, thus triggering the urge among the physicists to study this system [8]. WS_2 is a semiconductor with a band gap of 1.35 eV, thus expanding the light absorption region to infrared (IR) region, i.e. 910 nm [8]. The band gap of WS_2 can also be controlled from indirect to direct type by exfoliating the bulk WS_2 to nanosheets [14]. Nanoscale WS_2 has also demonstrated its potential use in advanced applications, such as photothermal therapy for destroying cancer cells by converting the absorbed near IR light into heat [8]. As a common, yet important application of WS_2, its use as a nano-photocatalyst is tremendous. In this regard, a few reports have highlighted photocatalytic studies of pure and WO_3-coupled WS_2 systems [15, 16]. Under UV illumination for 10 min, the mesoporous WS_2 nanosheets were shown to degrade rhodamine B (RhB) up to 21% [15]. In contrast, much enhanced photocatalytic degradation of phenol has been witnessed upon extended UV illumination of polycrystalline mixed WO_3/WS_2 systems [16].

The present work highlights hydrothermal synthesis of inorganic fullerene (IF)-type WS_2 nanoparticles and their photocatalytic responses considering both visible and UV exposure and with malachite green (MG) as the target agent. Structural, morphological, optical and Raman analyses have also been discussed.
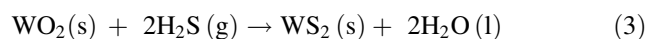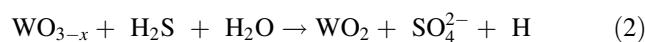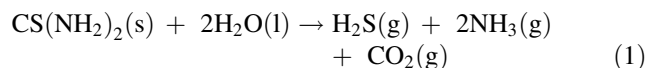
2 Experimental: materials and methods

2.1 Synthesis of inorganic fullerene-type nano-WS_2 system

We have attempted a two-step hydrothermal process for the production of nano-WS_2. The chemicals used in the synthesis were of analytical grade and have been used without further purification. While sodium tungstate (Na_2WO_4· $2H_2O$) (Rankem, 98% pure) has been considered as the source of tungsten, thiourea (CH_4N_2S) (Merck, 99% pure) was used as the source of sulfur. First, 1.64 g of sodium tungstate, 0.69 g of hydroxylamine hydrochloride (NH_2-OH·HCl) (Merck, 98% pure) and 1.52 g of thiourea are

dissolved in 30 ml of deionized Millipore® water. The mixture was kept under constant stirring for 25 min, with the pH value adjusted to 6 by adding few drops of ammonia water. The solution is transferred to a 50-ml teflon-lined stainless steel autoclave, which was properly sealed and then subjected to oven heating at a temperature of 180 °C, for 24 h. The collected product is washed several times with distilled water and then with ethanol under centrifugation (3500 rpm) for about 15 min. The precipitate obtained is oven dried at a temperature of 60 °C, for 10 h. The resultant product that appeared to be blonde yellow in color is labeled as S_1. The light colored powder obtained resembles that of an intermediate product (WO_{3-x}) in the formation of WS_2 which may arise due to the inadequacy of sulphur in the reaction process [17].

In the second step, 0.58 g of S_1 (obtained through the first step) is mixed with 0.78 g of thiourea and 40 ml deionized water in a conical flask and subjected to vigorous stirring for 20 min. Then, the solution is poured in a 50-ml Teflon-lined stainless steel autoclave, sealed airtight and kept in an oven maintained at a temperature of 200 °C, for 36 h. The product is centrifuged (3500 rpm, 5 min), washed with distilled water and finally, cleansed with ethanol suitably. The product is then dried in an oven (80 °C) for about 10 h. The steps as regards formation of the final nano-WS_2 product (S_2) is illustrated in Fig. 1. The chemical equations involved are as given below [17]:

$$CS(NH_2)_2(s) + 2H_2O(l) \rightarrow H_2S(g) + 2NH_3(g) + CO_2(g) \tag{1}$$

$$WO_{3-x} + H_2S + H_2O \rightarrow WO_2 + SO_4^{2-} + H \tag{2}$$

$$WO_2(s) + 2H_2S(g) \rightarrow WS_2(s) + 2H_2O(l) \tag{3}$$

2.2 Characterization techniques employed

To exploit the structural and crystallographic properties, X-ray diffraction (XRD) technique was employed using a MiniFlex Rigaku X-ray diffractometer equipped with a CuK_α source ($\lambda = 1.543$ Å). The morphological details of the as-synthesized WS_2 samples were revealed through scanning electron microscopy (JEOL, 6390LV) and transmission electron microscopy (FEI, Tecnai) imaging studies. The elemental composition of the samples was confirmed from the EDX spectra. On the other hand, luminescence characteristics and phonon-assisted vibrational modes are exploited through the luminescence spectrophotometer (Hitachi 2700 FL) and Raman spectrometer (Renishaw, Wottonunder-Edge); respectively. The optical absorption responses as obtained through UV–Vis spectroscopy (UV 2450, Shimadzu Corporation) are used for estimating energy band gap as well as photocatalytic degradation efficiency.

Fig. 1 Schematic diagram of the sequential steps involved in processing IF nano-WS$_2$ system
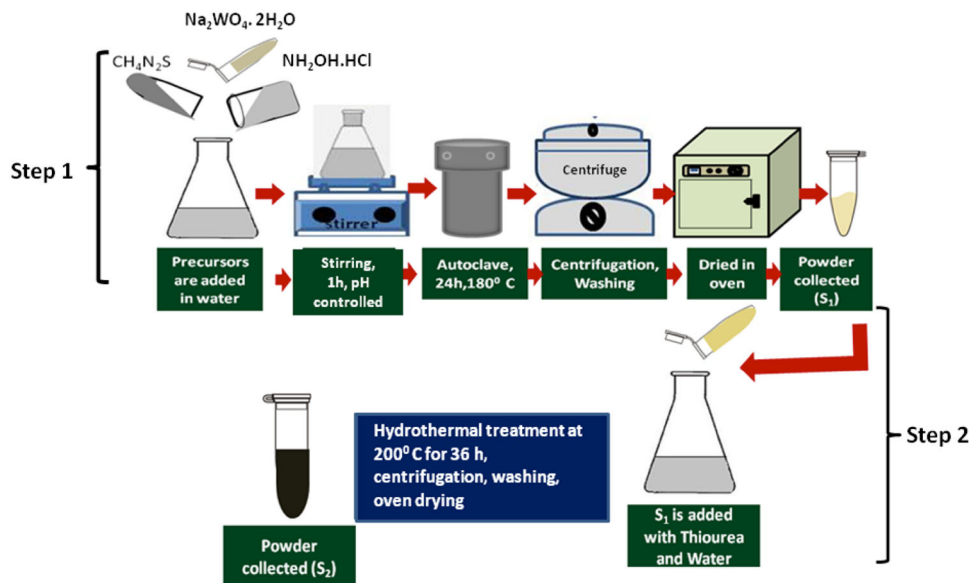
2.3 Execution of photocatalytic experiment

To analyze the photocatalytic efficiency of the as-prepared nano-WS$_2$ samples, we have chosen malachite green (MG) as the target to be decomposed. MG is an organic compound that is used as a dyestuff and controversially as an antimicrobial in aquaculture [18]. All around the globe, researchers are trying hard to find suitable ways to degrade harmful organic dyes and pollutants. The photoactivity of the nano-WS$_2$ samples has been investigated both under UV and day light illumination conditions. To perform the experiment, 100 mg/L of the WS$_2$ nanoparticles is first added to 30 mg/L of the MG, and then subjected to stirring for about 1 h in dark. In the next step, the mixture is ultrasonicated for about half an hour. The collected sol is then placed inside a cabinet which has the provision for UV lamp as well as the incandescent lamp, the latter being used as the source of visible light. The samples are placed on the base of the chamber at a distance of 12 cm from the UV source ($\lambda = 365$ nm) and the polychromatic visible light source used independently. The WS$_2$ nanocatalyst-loaded dye was irradiated for 15, 30, 45, 60 and 120 min. Next, 5 ml of the MG solution is taken for optical absorption analysis, knowing that the peak maxima for the initial absorption of MG appears at ~ 617 nm [19]. The percentage of decomposition of the MG under UV and visible light irradiation for various durations of UV exposure is given by:

$$\% \text{ degradation } = \left(\frac{C_0 - C_t}{C_0}\right) \times 100 \tag{4}$$

where, C_0 and C_t represent concentration of the MG solution before and after irradiation.

3 Results and discussion

3.1 Structural and morphological analyses

The XRD patterns of the as-prepared samples are shown in Fig. 2a, b. It can be seen that the sample S_1 exhibits diffraction peaks which is similar to that of WO$_3$.5H$_2$O (JCPDS File No. 44-0363) and WO$_3$.33H$_2$O (JCPDS File No. 35-1001) [17]. Attributed to (002) plane of hexagonal WS$_2$, the diffraction peak at $2\theta \sim 15.20°$ in sample S_1 is marginally shifted to 14.32° in system S_2 (JCPDS File No. 08-0237) [17]. The other peaks at 28.76°, 33.42°, 39.57°, 44.28°, 49.65° and 58.53° corresponded to (004), (101), (103), (006), (105) and (110) planes of the hexagonal WS$_2$, respectively. The sharp peaks corresponding to the (002) and (103) planes suggest competitive growth of the crystallites along these directions. The sharp diffraction lines are also shown in the figure in accordance with respective JCPDS files. From the analyses of diffractograms, it is quite apparent that the synthesized product obtained through the additional step ensured the desired phase of the nano-WS$_2$ system. The average crystallite size (D) of the WS$_2$ nanoparticles was calculated using the Williamson–Hall (W-H) plot by choosing the most prominent diffraction peaks, such as (004), (101), (103), (006), (105) and (110). The W-H expression is given by:

$$\beta \cos \theta = 4\varepsilon \sin \theta + 0.9\,\lambda/D, \tag{5}$$

where λ is the wavelength of the X-ray radiation ($\lambda = 0.1543$ nm for CuK_α line), 2θ is the diffraction angle, β is the line width at half maximum height and ε is the mean lattice strain. As found in Fig. 2b, by plotting $\beta \cos\theta$ vs. $4 \sin\theta$, the size component can be obtained directly from the intercept of the straight line on the y-axis [20].
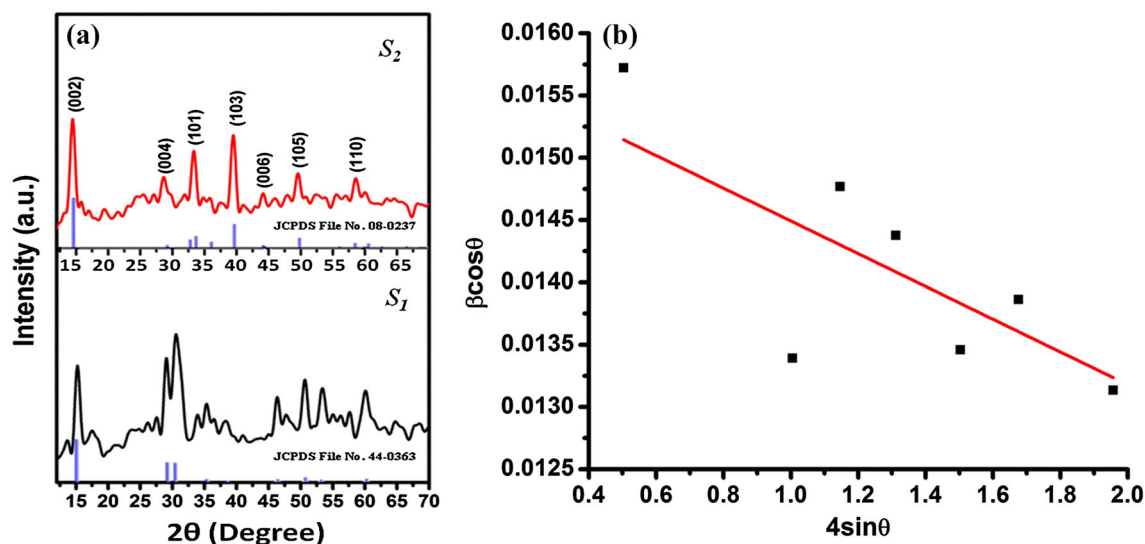
Fig. 2 **a** X-ray diffractograms of the prepared samples and **b** the W-H plot for sample S_2

Similarly, microstrain ε can be evaluated from the desired slope. Using the W-H formula, the average crystallite size was calculated to be ~ 7.7 nm and the microstrain as, -1.3×10^3. The negative strain corresponds to relaxed nature of the crystallites, whereas positive strain indicates compaction of the crystallites [21]. Using conditions relevant to hexagonal structure, the crystal lattice parameters can be found as, $a = b = 3.16$ Å and $c = 12.28$ Å.

The EDX spectra of the two samples S_1 and S_2 are shown in Fig. 3. The presence of elements W, O and S is evident from the EDX spectrum of S_1. However, the amount of sulphur present in S_1 is quite small. The amount of sulphur present is significantly high in sample S_2, as compared to S_1. Since no oxygen peak is witnessed in the EDX spectrum of sample S_2, it substantiates the development of high-yield WS_2 phase, free from oxide content. Moreover, the sample S_2 gave the atomic ratio of W to S as, 1:1.83. Since the formation of phase-pure WS_2 is ascertained, further characterization wrt imaging was considered for the sample S_2.

Figure 4A shows the SEM micrographs of the desired WS_2 nanosystem. Here, we could clearly notice formation of clustered nanoparticles similar to an earlier work [22]. In fact, the structural morphology of the WS_2 nanostructures largely depends on the reaction time and processing temperature [23]. The agglomeration of particles is caused due to the multi-nuclei attachment, which serves as the possible mechanism of growth along (002) direction [24]. The low and high magnification micrographs are shown in Fig. 4A(a), A(b), respectively. Figure 4B(a–d) depicts the TEM imaging feature of the nano-WS_2 system. Apparently, the TEM image reveals development of fullerene-shaped structures of nano-WS_2 system [Fig. 4B(a), (c)]. The size distribution is shown in the inset of Fig. 4B(a). The
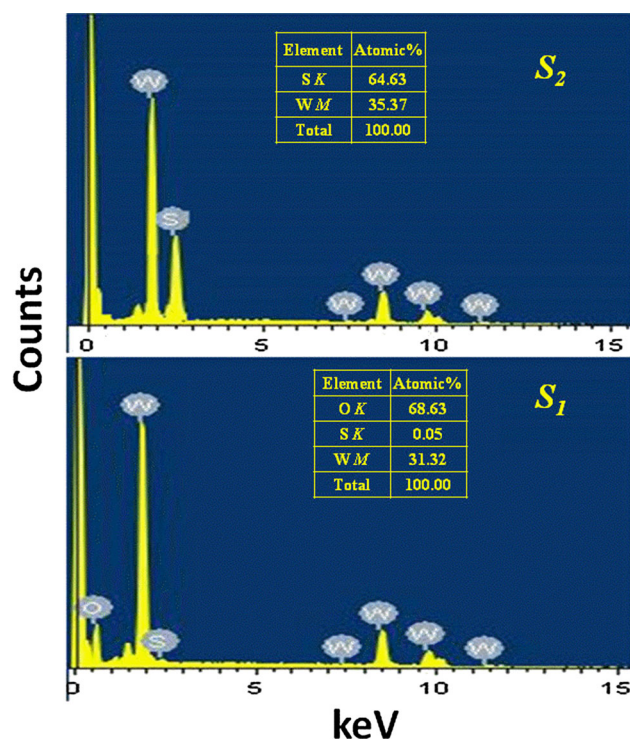

Fig. 3 EDX spectra of the as-prepared nano-WS_2 samples

formation of diffused rings as witnessed in the SAED micrograph [Fig. 4B(b)] suggests the polycrystalline nature of the synthesized product which could arise due to the presence of surface defects on nano-WS_2 system [25]. The hollow core IF fullerene-type structures with bent lattice edges can be found in Fig. 4B(c). In the magnified image of the corner of an individual IF structure we noticed that a corner is essentially formed from a series of bent lattice planes [Fig. 4B(d)]. In this regard, strain relief mechanism

Fig. 4 A SEM micrographs of the as-prepared nano-WS$_2$ system: **a** low magnification, **b** high magnification. **B a** TEM micrograph depicting distributed view of IF-type WS$_2$ nanoparticles with a histogram on size distribution (*inset*), **b** SAED pattern, **c** a single IF nano-WS$_2$ structure and **d** enlarged view of a segment showing the bent lattice structure of the WS$_2$ nanosystem
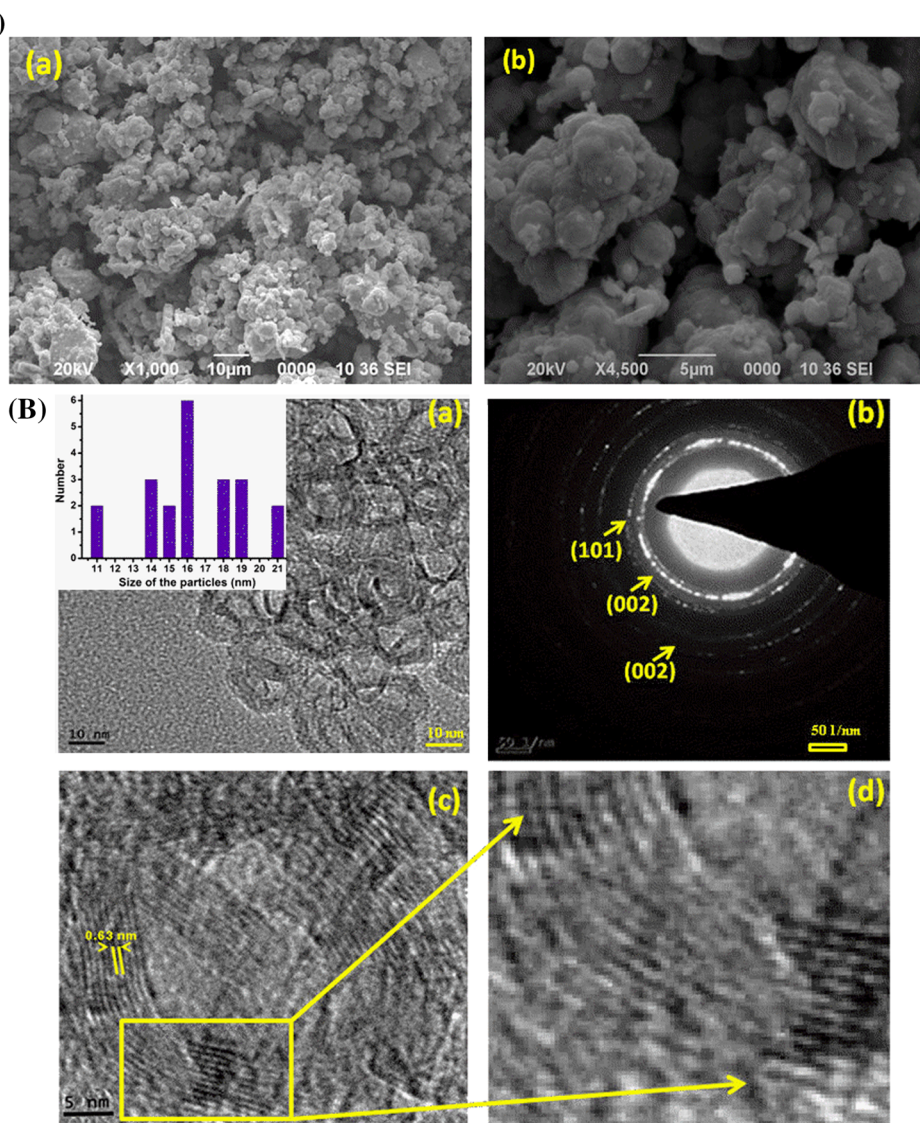
has been proposed for exhibition of such unusual morphology/structures [26]. The average outer diameter of the IF nano-WS$_2$ particles is estimated to be ∼16 nm, with an interlayer spacing of 0.63 nm.

3.2 Vibrational analysis using Raman and FTIR spectroscopy techniques

Figure 5a represents the Raman spectrum of the synthesized nano-WS$_2$ system measured with an excitation wavelength, λ_{ex} ∼514 nm. Raman spectroscopy is a non-invasive, yet important tool to reveal structural information as regards number of layers, defects, doping levels, strain effects and other factors. In fact, bulk WS$_2$ shows two major bands corresponding to E_{2g}^1 and A_{1g} modes essentially located at ∼351 and 420 cm^{-1}, respectively [27]. In our case, the two vibronic bands are witnessed at ∼352.4

and 419.5 cm^{-1} which correspond to the first-order modes at the Brillouin zone; with first being an in-plane mode E_{2g}^1 and second identified as out-of-plane mode A_{1g} [28]. These values are slightly different when compared to those of the bulk WS$_2$ crystal. The slight shift of A_{1g} mode towards higher wavelength side may be due to the decrease in interlayer Van der Waals interaction which causes weaker restoring forces in the vibration as we move from bulk to few layers of WS$_2$ [14]. On the other hand, the blue shift in E_{2g}^1 is attributed to the reduced long-range Coulomb interaction between the effective charges caused by an increase in the dielectric screening on stacking-induced changes in the interlayer bonding [14]. The ratio of intensities of the E_{2g}^1 and A_{1g} calculated stands at 0.61 which is higher than that of bulk WS$_2$ but lower than the mono, bi and tri-layered WS$_2$ nanosystems [29]. Thus our
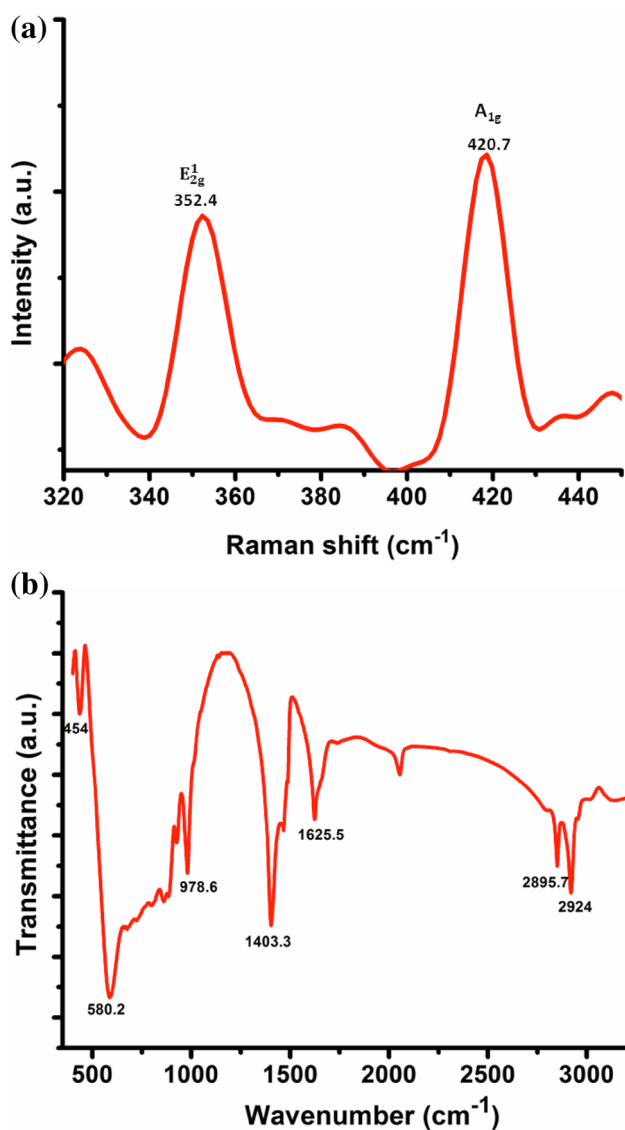
(a)

(b)

Fig. 5 **a** Raman spectrum and **b** FTIR spectrum of the as-prepared IF-type WS$_2$ nanosystem (sample S_2)

IF-type nano-WS$_2$ must comprise sufficient number of layers which results in a dominant out-of-plane vibration over the in-plane one.

The FTIR spectroscopy essentially offers information regarding the nature of chemical bonding and the molecular structure of the system under study. Figure 5b depicts the FTIR spectrum of the synthesized nano-WS$_2$ system in the wavenumber range 400–3200 cm^{-1}. A distinct band at 454 cm^{-1} refers to the characteristic S–S bond of the elemental sulphur [30]. The bands positioned at ~580.2 and 978.6 cm^{-1} are ascribed to the W−S bond and S–S bond, respectively [31]. The bands found at ~1403.3 and 1625.5 cm^{-1} are ascribed to the stretching vibrations of the hydroxyl group [31]. Moreover, the vibrational bands at

2895.7 and 2924 cm^{-1} can be attributed to the atmospheric OH and that is available in the WS$_2$ system [31].

3.3 Optical band gap calculation and luminescence response

The UV–Vis optical absorption spectrum of the sample S_2 is shown in Fig. 6a. It depicts presence of two weak absorption bands located at ~537 and ~649 nm. Even though these two bands represent characteristic absorption response of IF-WS$_2$ nanostructures [32, 33], particularly the peak at ~649 nm corresponds to d–d type transitions of the WS$_2$ at the center of the Brillouin zone [34]. To determine the band gap of the prepared WS$_2$ nanoparticles, we have plotted the Tauc's plot using the relation [31], $\alpha h v = (h v - E_g)^n$, where h is the Planck's constant, v is the
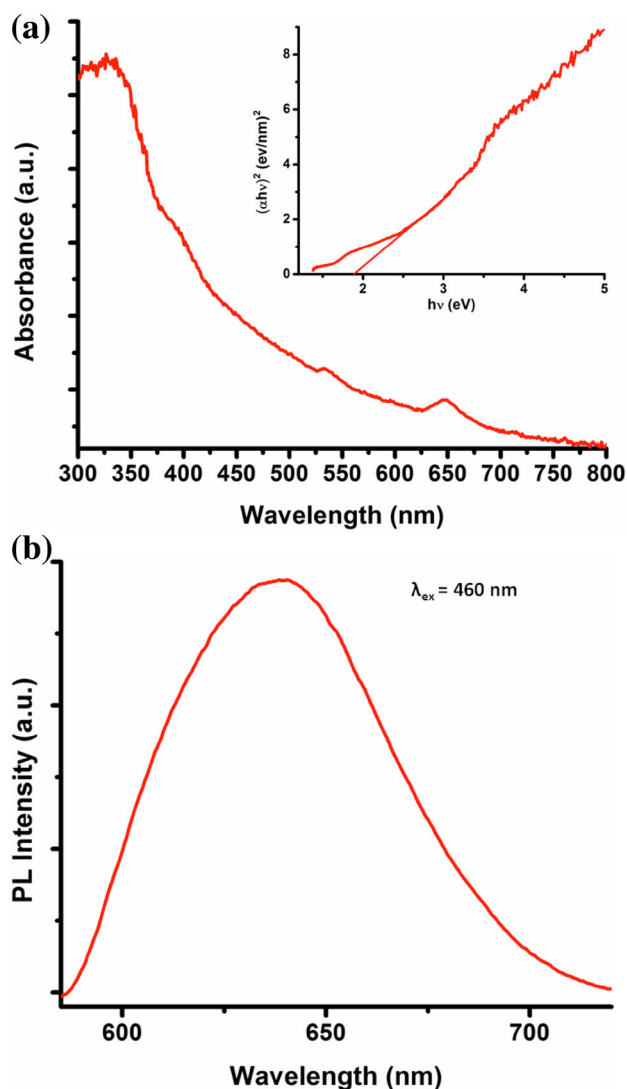
(a)

(b)

Fig. 6 **a** UV–Vis optical absorption spectrum along with the Tauc's plot (*inset*), and **b** PL spectrum of the IF nano-WS$_2$ system

frequency of the incident light and α is the absorption coefficient. Putting $n = \frac{1}{2}$ for the direct allowed transitions, the band gap of the prepared WS$_2$ nanosystem is estimated to be 1.91 eV, which is in good agreement with an earlier report [8].

PL is a versatile tool to exploit the radiative emission and defect-mediated transitions. PL spectroscopy study is necessary to understand the carrier recombination processes to be understood for photocatalysis in latter studies. Figure 6b shows the PL spectrum of the synthesized WS$_2$ nanosystem acquired under an excitation wavelength of $\lambda_{exc} = 460$ nm. The broad peak at ~ 638 nm is the outcome of transition from the indirect band gap type to the direct band gap one when the bulk system is thinned down to a few nanometric layers [14]. This peak suggests the separation efficiency of the electron–hole pairs, with superior characteristics due to the presence of surface area and active edges [19]. Reports suggest that a direct gap exists at the K points of the Brillouin zone between the spin-orbit split valence band and the doubly degenerate conduction band. The indirect band gap is known to form between a local conduction band which is minimum at the midpoint between Γ and K and the valence band is maximum at the Γ point [14]. The existence of the direct transition can be explained from excitonic radiative relaxation and accordingly, the appearance of PL peak has been observed at energies slightly lower than the 2.05 eV direct band gap of WS$_2$ [14]. The luminescence pattern is observed to be asymmetrically broadened and with a full-width half-maxima (FWHM) of approximately 183 meV. A broad emission peak suggests that, the transition from indirect to direct nature of the gap is not discrete, but continuous over an inseparable energy band.

3.4 Evaluation of photocatalytic performance of fullerene-type nano-WS$_2$ system

To investigate photoactivity of the IF WS$_2$ nanoparticles, we have chosen MG as the target agent under UV and visible light illumination conditions. The UV–Vis absorption response of the organic dye and nano-WS$_2$ catalyst-loaded MG can be found in Fig. 7a. The WS$_2$-loaded dye showed a steady fall in the absorbance with increasing the UV exposure time, exhibiting a minimal strength at ~ 617 nm. Conversely, the samples irradiated under visible light showed a rapid drop in the absorbance response as compared to the samples subjected to UV light (Fig. 7a, b). The IF WS$_2$ nanoparticles tend to exhibit better catalytic efficiency under visible light because of the narrow band gap, which acts as a driving force to activate the redox reaction necessary for the production of hydroxyl radicals [8]. Also, it has been reported that irregular hexagonal-type structures with ample surface defects served the purpose of a good nanocatalyst under visible light illumination [35]. Also, IF-type particles can have enhanced photocatalytic responses because of the strong optical absorption, large surface area, and documented chemical inertness under illumination [36].

The schematic diagram as regards the mechanism of the photocatalytic activity of the synthesized WS$_2$ nanosystem is shown in Fig. 8. The host WS$_2$ nanocatalyst, upon light irradiation would release electrons and holes. The excited electrons are likely to move to the conduction band creating adequate holes in the valence band. These generated charge carriers are likely to be trapped in the active W^{4+} and S^{2-} defect sites lest they might recombine with the counterparts to dissipate energy. These carriers would migrate to the nanocatalyst surfaces, resulting in the formation of reactive intermediates. The photoinduced holes and the reactive hydroxyl radicals are profoundly responsible for initiating the redox reaction required for decomposition of the harmful dye/organic pollutant. The hydroxyl radical is produced either by decomposition of water or by a hole reacting with the OH$^-$. Since the target MG is in aqueous form; therefore, the water molecule is believed to come in contact with the surface of the nanocatalyst. The OH group or O^{2-} is likely to be trapped by the active sites of the nanocatalyst [37]. The oxygen vacancy centers are easily de-trapped and the electrons are transferred to the adsorbed oxygen which produces the superoxide radicals [38]. Water and hydroxyl ions are transformed to the hydroxyl radicals by the photo-generated holes [39]. These superoxide and hydroxyl radicals being very strong oxidizing agents could easily degrade the complete dye to its constituent products [40]. We observed an increasing trend of degradation of the MG on increasing the irradiation time. As high as 45% decomposition has been witnessed on irradiating the catalyst-loaded dye under UV light for 120 min (Fig. 7c). Conversely, the IF-WS$_2$ nanocatalyst gives a superbly enhanced decomposition of MG ($\sim 71.2\%$) when subjected to visible light irradiation for 120 min (Fig. 7c). For the sake of comparison, the photocatalytic responses of different MoS$_2$ and WS$_2$ nanosystems are presented in Table 1. To name a few, WS$_2$ nanosheets possess excellent photocatalytic activity over the complete spectrum, from UV to NIR [8]. Also, mesoporous WS$_2$ nanosheets are shown to be highly stable and efficient even after four cycles of RhB degradation [15]. In case of degradation of phenol by WO$_3$/WS$_2$ polycrystalline powders, the photoactivity is highly dependent on the molar ratio of the systems used [16]. Similarly, WS$_2$/TiO$_2$ has also shown an improved photocatalytic activity on harmful organic dyes, such as, target MO [41]. In this
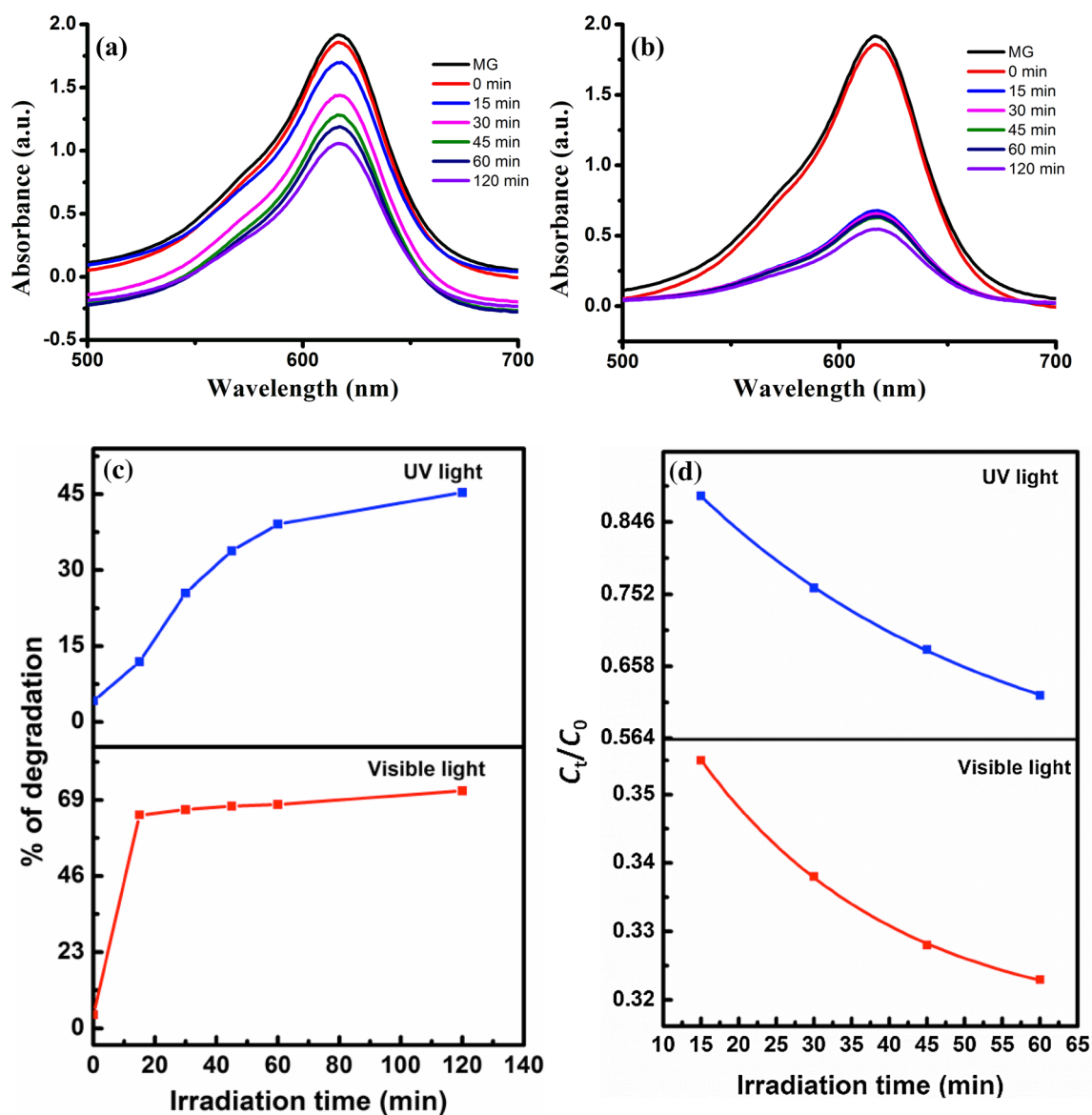
Fig. 7 UV–Vis absorption spectra of MG and IF nano-WS$_2$ catalyst-loaded dye with different irradiation times: **a** UV illumination, **b** visible light illumination. The percentage of degradation and pseudo-first-order plots under aforesaid conditions are shown in **c**, **d** on a comparative basis

regard, IF-type WS$_2$ systems, which are rarely discussed in the literature, find its importance in the list of nanocatalysts. The performance of IF-type WS$_2$ nanosystem on the degradation of MG dye is evaluated through simple kinetics, as discussed below.

The kinetics of photocatalytic degradation of MG at the nanocatalyst surface can be understood through Langmuir–Hinshelwood (L-H) model [42]. For a dilute solution (mM) ($C \ll 1$), it can be expressed in the form of a first-order reaction given by [42]:

$$C_t = C_0 e^{-k_a t}. \tag{6}$$

Here, C_0 is the initial concentration of the MG solution, t is the irradiation time and k_a is the pseudo-first-

order rate constant. At $t = t_0$, $C = C_0$, the initial concentration of the target before irradiation. The percentage degradation of MG is represented in Fig. 7c. The plots of C_t/C_0 versus t, for UV and visible light conditions are shown in Fig. 7d. The plots essentially help to predict the pseudo-first-order rate constant, k_a. The rate constants, as obtained directly from the graphs (Fig. 7d), are calculated to be 0.0239 and 0.0414 min^{-1} for IF nano-WS$_2$ samples exposed to UV light and visible light, respectively. A higher rate constant for the latter case, suggests that our IF nano-WS$_2$ are capable of displaying improved photoactivity under visible light illumination than that of UV exposure.

Fig. 8 Schematic of the photocatalytic mechanism expected in the IF nano-WS$_2$ system
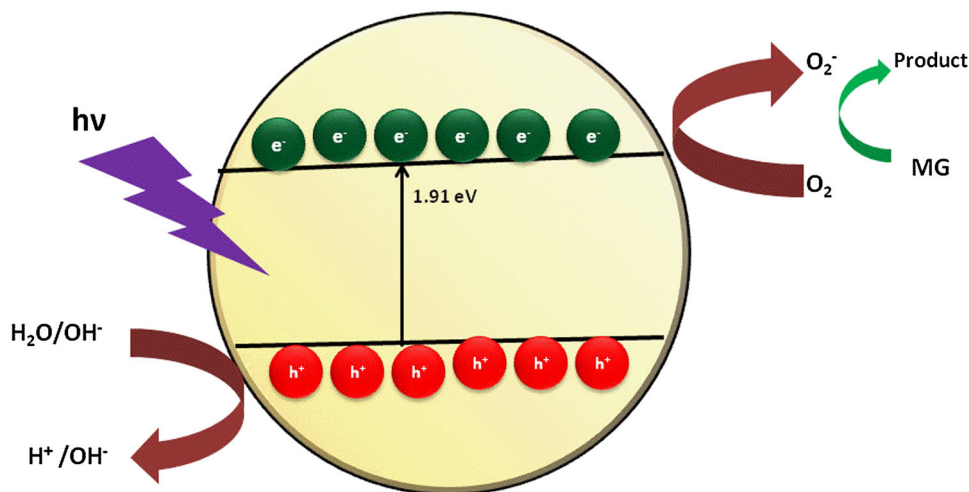

Table 1 A comparative view as regards photocatalytic performance of different nanophotocatalysts (RhB: rhodamine B, MO: methyl orange, CR: congo red, MG: malachite green)

Sl. no.	Material	Illumination source	Target	Degradation time and amount	References
1	SnO$_2$/MoS$_2$ nanocomposite	UV light	RhB	50 min (100%)	[9]
2	TiO$_2$/MoS$_2$ @ zeolite	Visible light	MO	60 min (95%)	[10]
3	WS$_2$ nanosheets	UV light	MO	100 min (100%)	[8]
4	WS$_2$ nanosheets	Visible light	MO	300 min (90%)	[8]
5	Mesoporous WS$_2$ nanosheets	UV light	RhB	10 min (21%)	[15]
6	WO$_3$/WS$_2$ polycrystalline powder	UV light	Phenol	480 min (80%)	[16]
7	WS$_2$/C-dot hybrid nanosheets	Visible light	CR	10 min (12%)	[28]
8	WS$_2$/TiO$_2$ nanosystem	Visible light	MO	60 min (95%)	[41]
9	IF-WS$_2$ nanosystem	UV light	MG	120 min (45%)	This work
10	IF-WS$_2$ nanosystem	Visible light	MG	120 min (71.2%)	This work

4 Conclusion

We have demonstrated a user friendly synthesis and photocatalytic activity of IF-type WS$_2$ nanoparticles. The hexagonal crystal structure of WS$_2$ is evident from XRD analysis. The presence of elements W and S has been confirmed from the EDX spectra. The direct band gap of the nano-WS$_2$, as predicted from the Tauc's plot, is $\sim$1.91 eV. The single distinct peak at 630 nm corresponds to the transition of the band structures from the indirect to direct band gap type. On the other hand, Raman spectrum reveals the presence of one in-plane E_{2g}^1 mode and one A_{1g} out-of-plane mode. The formation of IF-type nanoparticles with an average outer diameter of 16 nm has been observed through the electron micrographs. The photocatalytic efficiency of the synthesized IF WS$_2$ nanocatalyst under visible light illumination gave a maximum degradation of 71.2% as compared to 45% when illuminated by UV light. Photoactivity studies of TMDCs with inclusion of suitable dopants and radiation effects are in progress.

References

1. K.S. Novoselov, A.K. Geim, S.V. Morozov, D. Jiang, Y. Zhang, S.V. Dubonos, I.V. Grigorieva, A.A. Firsov, Electric field effect in atomically thin carbon films. Science **306**, 666–669 (2004)
2. H. Tian, W. Mi, X.-F. Wang, H. Zhao, Q.-Y. Xie, C. Li, Y.-X. Li, Y. Yang, T.-L. Ren, Graphene dynamic synapse with modulatable plasticity. Nano Lett. **15**, 8013–8019 (2015)
3. H. Tian, H. Zhao, X.F. Wang, Q.Y. Xie, H.Y. Chen, M.A. Mohammad, C. Li, W.T. Mi, Z. Bie, C.H. Yeh, Y. Yang, H.S. Philip Wong, P.W. Chiu, T.L. Ren, In situ tuning of switching window in a gate-controlled bilayer graphene-electrode resistive memory device. Adv. Mater. **27**, 7767–7774 (2015)
4. Q.H. Wang, K.K. Zadeh, A. Kis, J.N. Coleman, M.S. Strano, Electronics and optoelectronics of two-dimensional transition metal dichalcogenides. Nat Nanotechnol **7**, 699–712 (2012)
5. S. Bhattacharyya, A.K. Singh, Semiconductor-metal transition in semiconducting bilayer sheets of transition-metal dichalcogenides. Phys. Rev. B. **86**, 075454 (2012)

6. H. Tian, M.L. Chin, S. Najmaei, Q. Guo, F. Xia, H. Wang, M. Dubey, Optoelectronic devices based on two-dimensional transition metal dichalcogenides. Nano Res. **9**, 1543–1560 (2016)

7. H. Tian, J. Tice, R. Fei, V. Tran, X. Yan, L. Yang, H. Wang, Low-symmetry two-dimensional materials for electronic and photonic applications. Nano Today **11**, 763–777 (2016)

8. Y. Sang, Z. Zhao, M. Zhao, P. Hao, Y. Leng, H. Liu, From UV to near-infrared, WS_2 nanosheet: a novel photocatalyst for full solar light spectrum photodegradation. Adv. Mater. **27**, 363–369 (2015)

9. S.V.P. Vattikuti, C. Byon, C.V. Reddy, R.V.S.S.N. Ravikumar, Improved photocatalytic activity of MoS_2 nanosheets decorated with SnO_2 nanoparticles. RSC Adv. **5**, 86675–86684 (2015)

10. W. Zhang, X. Xiao, L. Zheng, C. Wan, Fabrication of TiO_2/MoS_2@zeolite photocatalyst and its photocatalytic activity for degradation of methyl orange under visible light. Appl. Surf. Sci. **358**, 468–478 (2015)

11. D. Voiry, H. Yamaguchi, J. Li, R. Silva, D.C.B Alves, T. Fujita, M.W. Chen, T. Asefa, V.B. Shenoy, G. Eda, M. Chhowalla, Enhanced catalytic activity in strained chemically exfoliated WS_2 nanosheets for hydrogen evolution. Nat. Mater. **12**, 850 (2013)

12. L. Rapoport, Y. Bilik, Y. Feldman, M. Homyonfer, S.R. Cohen, R. Tenne, Hollow nanoparticles of WS_2 as potential solid-state lubricants. Nature **387**, 791–793 (1997)

13. R. Levi, O. Bitton, G. Leitus, R. Tenne, E. Joselevich, Field-effect transistors based on WS_2 nanotubes with high current-carrying capacity. Nano Lett. **13**, 3736–3741 (2013)

14. H.R. Gutierrez, N. Perea-Lopez, A.L. Elias, A. Berkdemir, B. Wang, R. Lv, F. Lopez-Urias, V.H. Crespi, H. Terrones, M. Terrones, Extraordinary room-temperature photoluminescence in triangular WS_2 monolayers. Nano Lett. **13**, 3447–3454 (2013)

15. S.V.P. Vattikuti, C. Byon, C.V. Reddy, Preparation and improved photocatalytic activity of mesoporous WS_2 using combined hydrothermal-evaporation induced self-assembly method. Mater. Res. Bull. **75**, 193–203 (2016)

16. A. Di Paola, L. Palmisano, V. Augugliaro, Photocatalytic behavior of mixed WO_3/WS_2 powders. Catal. Today **58**, 141–149 (2000)

17. Y. Shang, J. Xia, Z. Xu, W. Chen, Hydrothermal synthesis and characterization of quasi 1D tungsten disulfide nanocrystal. J. Disp. Sci. Technol. **26**, 635–639 (2005)

18. S. Srivastava, R. Sinha, D. Roy, Toxicological effects of malachite green. Aquat. Toxicol. **66**, 319–329 (2004)

19. G. Parshetti, S. Kalme, G. Saratale, S. Govindwar, Biodegradation of Malachite Green by *Kocuria rosea MTCC* 1532. Acta Chim. Slov. **53**, 492–498 (2006)

20. S.W. Park, J.T. Jang, J. Cheon, H.H. Lee, D.R. Lee, Y. Lee, Shape dependent compressibility of TiO_2 anatase nanoparticles. J. Phys. Chem. C **112**(26), 9627–9631 (2008)

21. S. Hazarika, D. Mohanta, Extraction and characterization of mixed phase KNO_2–KNO_3 nanocrystals derived from flat-leaf green spinach. Phys. Scr. **87**, 015603-1–5 (2013)

22. E. García-Lecina, I. García-Urrutia, J.A. Díez, J. Fornell, E. Pellicer, J. Sort, Codeposition of inorganic fullerene-like WS_2 nanoparticles in an electrodeposited nickel matrix under the influence of ultrasonic agitation. Electrochim. Acta **114**, 859–867 (2013)

23. S. Cao, T. Liu, S. Hussain, W. Zeng, X. Peng, F. Pan, Mater. Lett. **129**, 205–208 (2014)

24. J.L. Elechiguerra, J. Reyes-Gasga, M. Jose-Yacaman, The role of twinning in shape evolution of anisotropic noble metal nanostructure. J. Mater. Chem. **16**, 3906–3919 (2006)

25. Yu Zhang, Y. Zhang, Q. Ji, J. Ju, H. Yuan, J. Shi, T. Gao, D. Ma, M. Liu, Y. Chen, X. Song, H.Y. Hwang, Y. Cui, Z. Liu, Controlled growth of high-quality monolayer WS_2 layers on sapphire and imaging its grain boundary. ACS Nano **7**, 8963–8971 (2013)

26. C. Schuffenhauer, R. Popovitz-Biro, R. Tenne, Synthesis of NbS_2 nanoparticles with (nested) fullerene-like structure (IF). J. Mater. Chem. **12**, 1587–1591 (2002)

27. H. Zeng, G-B. Liu, J. Dai, Y. Yan, B. Zhu, R. He, L. Xie, S. Xu, X. Chen, W. Yao, X. Cui, Optical signature of symmetry variations and spin-valley coupling in atomically thin tungsten dichalcogenides. Sci. Rep. **3**, 1608 (2013)

28. P. Atkin, T. Daeneke, Y. Wang, B.J. Carey, K.J. Berean, R.M. Clark, J.Z. Ou, A. Trinchi, I.S. Cole, K. Kalantar-zadeh, 2D WS_2/carbon dot hybrids with enhanced photocatalytic activity. J. Mater. Chem. A **4**, 13563–13571 (2016)

29. A. Berkdemir, H.R. Gutiérrez, A.R. Botello-Méndez, N. Perea-López, A.L. Elías, C.I. Chia, B. Wang, V.H. Crespi, F. López-Urías, J.C. Charlier, H. Terrones, M. Terrones, Identification of individual and few layers of WS_2 using Raman spectroscopy. Sci. Rep. **3**, 1755 (2013)

30. J. Coates, Interpretation of infrared spectra, a practical approach in encyclopedia of analytical chemistry, ed. R.A. Meyers (Wiley, Chichester, 2000), p. 10829

31. S.V.P. Vattikuti, C. Byon, Effect of CTAB surfactant on textural, structural, and photocatalytic properties of mesoporous WS_2. Sci. Adv. Mater. **7**(12), 2639–2645 (2015)

32. Y. Feldman, G.L. Frey, M. Homyonfer, V. Lyakhovitskaya, L. Margulis, H. Cohen, G. Hodes, J.L. Hutchison, R. Tenne, Bulk synthesis of inorganic fullerene-like MS_2 (M = Mo, W) from the respective trioxides and the reaction mechanism. J. Am. Chem. Soc. **118**, 5362–5367 (1996)

33. G.L. Frey, S. Elani, M. Homyonfer, Y. Feldman, R. Tenne, Optical-absorption spectra of inorganic fullerene like MS_2 (M=Mo, W). Phys. Rev. B **57**, 6666 (1998)

34. S.M. Notley, High yield production of photoluminescent tungsten disulphide nanoparticles. J. Coll. Interf. Sci. **396**, 160–164 (2013)

35. S.V.P. Vattikuti, C. Byon, V. Chitturi, Selective hydrothermally synthesis of hexagonal WS2 platelets and their photocatalytic performance under visible light irradiation. Superlattices Microstruct. **94**, 39–50 (2016)

36. H. Tributsch, *Structure and bonding*, vol. 49 (Springer, Berlin, 1982), p. 127

37. N. Paul, A. Deka, D. Mohanta, Augmented photocatalytic activity and luminescence response of Tb^{3+} doped nanoscale titania systems. J. Appl. Phys. **116**, 144902-1–7 (2014)

38. S. Bingham, W.A. Daoud, Recent advances in making nano-sized TiO_2 visible-light active through rare-earth metal doping. J. Mater. Chem. **21**, 2041–2050 (2011)

39. K.M. Parida, N. Sahu, Visible light induced photocatalytic activity of rare earth titania nanocomposites. J. Mol. Catal. A **287**, 151–158 (2008)

40. T. Peng, D. Zhao, H. Song, C. Yan, Preparation of lanthana-doped titania nanoparticles with anatase mesoporous walls and high photocatalytic activity. J. Mol. Catal. A **238**, 119–126 (2005)

41. L. Zheng, W. Zhang, X. Xiao, Preparation of titanium dioxide/tungsten disulfide composite photocatalysts with enhanced photocatalytic activity under visible light. Korean J. Chem. Eng. **33**, 107–113 (2016)

42. U.I. Gaya, A.H. Abdullah, Heterogeneous photocatalytic degradation of organic contaminants over titanium dioxide: a review of fundamentals, progress and problems. J. Photochem. Photobiol. C **9**, 1–12 (2008)